Simultaneous generation of direct- and indirect-gap photoluminescence in multilayer MoS₂ bubbles

Hailan Luo,[1,2,*] Xuanyi Li,[1,2,*] Yanchong Zhao,[1,2,*] Rong Yang,[1] Lihong Bao,[1] Yufeng Hao,[3,4] Yu-nan Gao,[5] Norman N. Shi,[6] Yang Guo,[1] Guodong Liu,[1] Lin Zhao,[1] Qingyan Wang,[1] Zhongshan Zhang,[1] Guangyu Zhang,[1,2,7] Jiatao Sun,[1,8,†] Yuan Huang,[1,7,‡] Hongjun Gao,[1,2] and Xingjiang Zhou [1,2,7,9,§]

[1]*Beijing National Laboratory for Condensed Matter Physics, Institute of Physics, Chinese Academy of Sciences, Beijing 100190, China*
[2]*School of Physical Sciences, University of Chinese Academy of Sciences, Beijing 100049, China*
[3]*National Laboratory of Solid State Microstructures, College of Engineering and Applied Sciences, Jiangsu Key Laboratory of Artificial Functional Materials and Collaborative Innovation Center of Advanced Microstructures, Nanjing University, Nanjing 210093, China*
[4]*Haian Institute of New Technology, Nanjing University, Haian 226600, China*
[5]*State Key Laboratory for Mesoscopic Physics, School of Physics, Peking University, Beijing 100871, China*
[6]*Department of Applied Physics and Applied Mathematics, Columbia University, New York 10027, USA*
[7]*Songshan Lake Materials Laboratory, Dongguan 523808, China*
[8]*School of Information and Electronics, MIIT Key Laboratory for Low-Dimensional Quantum Structure and Devices, Beijing Institute of Technology, Beijing 100081, China*
[9]*Beijing Academy of Quantum Information Sciences, Beijing 100193, China*

Transition metal dichalcogenide (TMD) materials have received enormous attention due to their extraordinary optical and electrical properties, with MoS₂ being one of the most representative examples. As the thickness increases from monolayer to multilayer, the photoluminescence (PL) of MoS₂ is gradually quenched due to the direct-to-indirect band gap transition. How to enhance PL response and decrease the layer dependence in multilayer MoS₂ remains a challenge. In this work, we report simultaneous generation of three PL peaks at around 1.3, 1.4, and 1.8 eV on multilayer MoS₂ bubbles. The temperature dependent PL measurements indicate that the two peaks at 1.3 and 1.4 eV come from phonon-assisted indirect-gap transitions while the peak at 1.8 eV comes from the direct-gap transition. The weakening of interlayer coupling on multilayer MoS₂ bubbles, which may account for the emergence of PL peaks, is confirmed by the low-frequency Raman spectroscopy. Using first-principles calculations, the band structure evolution of multilayer MoS₂ under strain is studied, from which the origin of the three PL peaks of MoS₂ bubbles is further confirmed. Moreover, PL standing waves are observed in MoS₂ bubbles that create Newton-Ring-like patterns. This work demonstrates that the bubble structure may provide new opportunities for engineering the electronic structure and optical properties of layered materials.

I. INTRODUCTION

Ultrathin two-dimensional (2D) materials exhibit fascinating electrical, optical, and mechanical performance. How to control and utilize their properties is important for various applications. MoS₂, as one of the most well-studied 2D semiconductors, shows high on-off ratio in field-effect transistor and strong photoluminescence (PL), which has great potential in logic circuit, photodetector, and flexible/wearable devices [1–5]. In the past decade, much attention has been focused on exploring the band structure and optical properties of monolayer and bilayer MoS₂ [6,7]. Some multilayer-related properties, such as photoluminescence, are rarely reported. While the direct band gap nature of monolayer MoS₂ is important for its application in photoelectric devices, its layer dependence also brings challenges during material synthesis.

If the unique properties in monolayer can also be realized in multilayer MoS₂, the processes of material synthesis and device fabrication will be greatly simplified. However, the goal for eliminating layer dependence is still a challenge in the 2D materials society. One strategy to prepare monolayerlike multilayer is to weaken interlayer coupling by strain engineering [8,9]. Bubble structure as recently used in strain engineering can provide a nonuniform strain field on layered materials [10–17], which serves as an inspiration for decoupling the interlayer interaction in multilayer MoS₂, as well as other multilayer TMD materials.

II. RESULTS

In this work, large size multilayer MoS₂ bubbles are fabricated on 300 nm SiO₂/Si substrate by a modified mechanical exfoliation technique [18]. Interestingly, while there is no PL signal on the flat region, three main PL peaks at 1.3 eV, 1.4 eV, and 1.8 eV are clearly detected on multilayer MoS₂ bubbles. PL oscillations induced by optical standing waves are observed on multilayer MoS₂ bubbles. The origin of the three PL peaks is unambiguously identified by temperature-
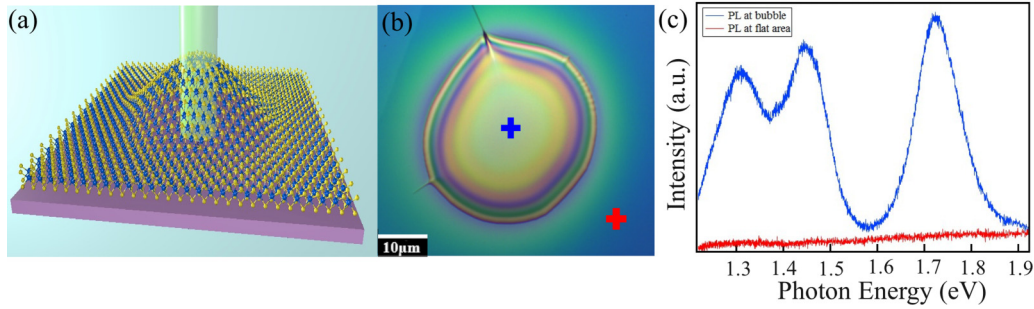

FIG. 1. PL response on multilayer MoS_2 bubble. (a) Schematic diagram of a MoS_2 bubble exfoliated onto Si wafer with 532 nm laser beam irradiating on it. (b) Optical microscopy image of one multilayer MoS_2 bubble on SiO_2/Si substrate showing Newton rings. (c) PL spectra measured on MoS_2 bubble center (red curve) and the flat region (blue curve) respectively. The measuring positions are marked by blue and red crosses in (b).

dependent PL measurements. The two lower energy PL peaks are phonon-assisted indirect gap transitions, which only emerge at high temperature (>60 K). The PL peak at 1.8 eV can be continuously observed as the temperature decreases to 20 K, confirming it is a direct band transition. First-principles calculation results unveil the electronic structure changes of multilayer MoS_2 under biaxial strain.

III. EXPERIMENT

Figures 1(a) and 1(b) show the schematic and optical microscope images of a typical MoS_2 bubble with lateral size of ∼40 μm exfoliated on SiO_2/Si substrate. Newton ring patterns caused by white light interference are clearly visible. Large MoS_2 bubbles with diameters up to 60 μm can be obtained [Fig. 3(a)], which are much larger than other MoS_2 bubbles transferred onto hole-array substrates [19–21]. Limited by the bubble sizes in previous reported studies [15–17], some exotic phenomena such as Raman and PL oscillation are observed and reported in this study. These results further emphasize the importance of larger size bubbles for enabling the exploration of various new properties of layered materials. The thickness of this flake has been characterized by atomic force microscope (AFM) as shown in Fig. S1 (∼8 nm) [22], from which the number of MoS_2 layers can be determined (∼13 layers). Tensile strain (up to 2.1%) in few-layer MoS_2 bubble samples have been confirmed by AFM measurement (Fig. S2). Compared with monolayer MoS_2 bubbles transferred on hole-array substrates [19–21], multilayer MoS_2 bubbles exfoliated on flat SiO_2/Si substrate can sustain higher pressure difference, which helps to enable large bubbles to sustain larger strain. It is also worth pointing out that the shape of these MoS_2 bubbles can stay intact after one year. The outstanding stability of these MoS_2 bubbles shows a promising prospect for applications, such as microlens.

Figure 1(c) shows the PL spectra of the multilayer MoS_2 bubble. Three PL peaks at 1.30, 1.45, and 1.74 eV are clearly detected on the bubble area. As expected, no clear PL signal can be observed on flat multilayer MoS_2 area because of the indirect band gap nature of multilayer MoS_2. The emergence of PL on multilayer MoS_2 bubble can be explained with the interlayer coupling change.

Figures 2(a) and 2(b) show the optical and PL mapping images of five MoS_2 bubbles, integrated at 1.75 eV. From

the PL intensity mapping images, we can clearly see that the oscillation behavior on MoS_2 bubble gradually emerges as the size of bubble increases. The oscillation phenomenon originates from the standing waves formed by the interference of incident and reflected beams at the MoS_2-substrate interface. Similar oscillation behaviors were discovered in Raman mapping images of graphene bubbles [12]. However, there are some distinct differences between graphene and MoS_2 bubbles. Graphene is a semimetal while MoS_2 is a semiconductor, where the latter can show more PL induced effects. To identify the origin of PL oscillation, PL mappings are displayed in Fig. 2(b) and Fig. S3. It can be found that the PL ring's diameters and ring numbers are different in these images integrated at 1.3 eV, 1.4 eV, and 1.7 eV. First, we extract 19 PL spectra along the yellow dashed line as indicated on the third bubble shown in Fig. 2(b), which all show three distinct PL peaks in each spectrum [Fig. 2(c)]. The PL intensity oscillation and peak position (∼1.75 eV) of the bubble can be extracted, as shown in Fig. 2(d). For this bubble, the diameter is 45 μm, and its height is ∼1.4 μm [the inset of Fig. 2(e)]. Figure 2(e) shows the calculated positions of interference maxima on the bubble. We find that the calculated positions of the bright rings fit well with the observed results, which confirms that the luminescence (708 nm, 1.75 eV) emitting from the bubble and the luminescence reflected from the SiO_2/Si surface generate the interference rings. More evidences can be referred to Fig. S3, which show the PL ring positions around 867 nm (1.43 eV) and 932 nm (1.33 eV), respectively. Therefore, the PL oscillation in the image is attributed to the interference of PL and not from the incident laser. From the PL image, we know that the height difference between two bright rings is λ/2. More supporting information is presented in Fig. S4 and Fig. S5.

To further distinguish the nature of the direct and indirect gap transitions in the multilayer MoS_2 bubbles, we performed temperature dependent PL measurements on MoS_2 bubbles from 20 K to 300 K (shown in Fig. 3 and Fig. S6). The PL peak at ∼1.8 eV can be clearly observed on the MoS_2 bubble between 20 K and 300 K. The PL peak at ∼1.3 eV becomes detectable only when temperature is higher than 60 K. The other PL peak at ∼1.4 eV starts to emerge as temperature increases to 150 K. Both peaks at ∼1.3 eV and ∼1.4 eV become more prominent as temperature increases. This result indicates that the transition process for the PL at ∼1.3 eV needs less
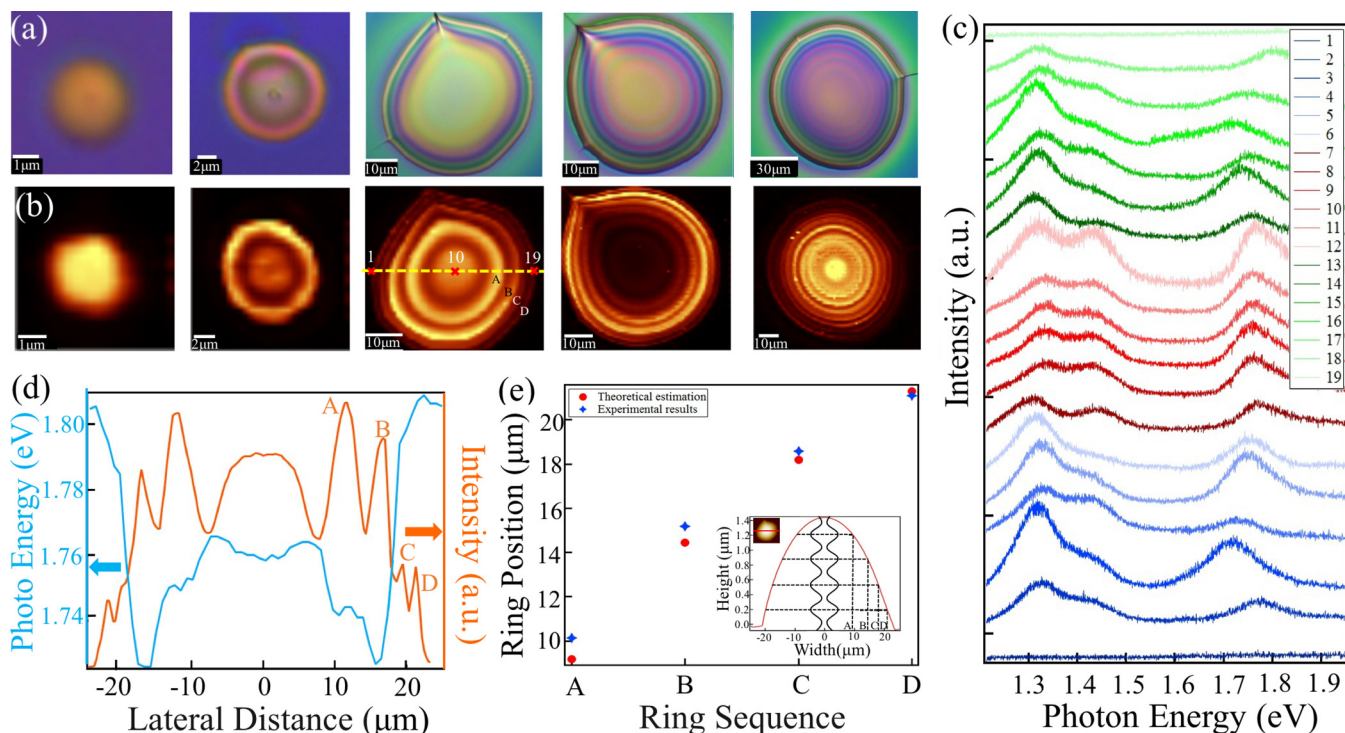
FIG. 2. PL oscillation behavior on multilayer MoS$_2$ bubble. (a) and (b) are optical images and PL mapping images of five different multilayer MoS$_2$ bubbles. PL intensity mapping images are integrated at 1.75 eV (integration energy window: 0.1 eV). (c) PL spectra extracted across the third bubble's center, which are collected along the yellow dashed line shown in (a). (d) The oscillation of PL intensity and PL peak position of the third MoS$_2$ bubble in (b). (e) Calculated position of interference maxima on the third bubble in (b). The inset in (e) is the height profile of the bubble.
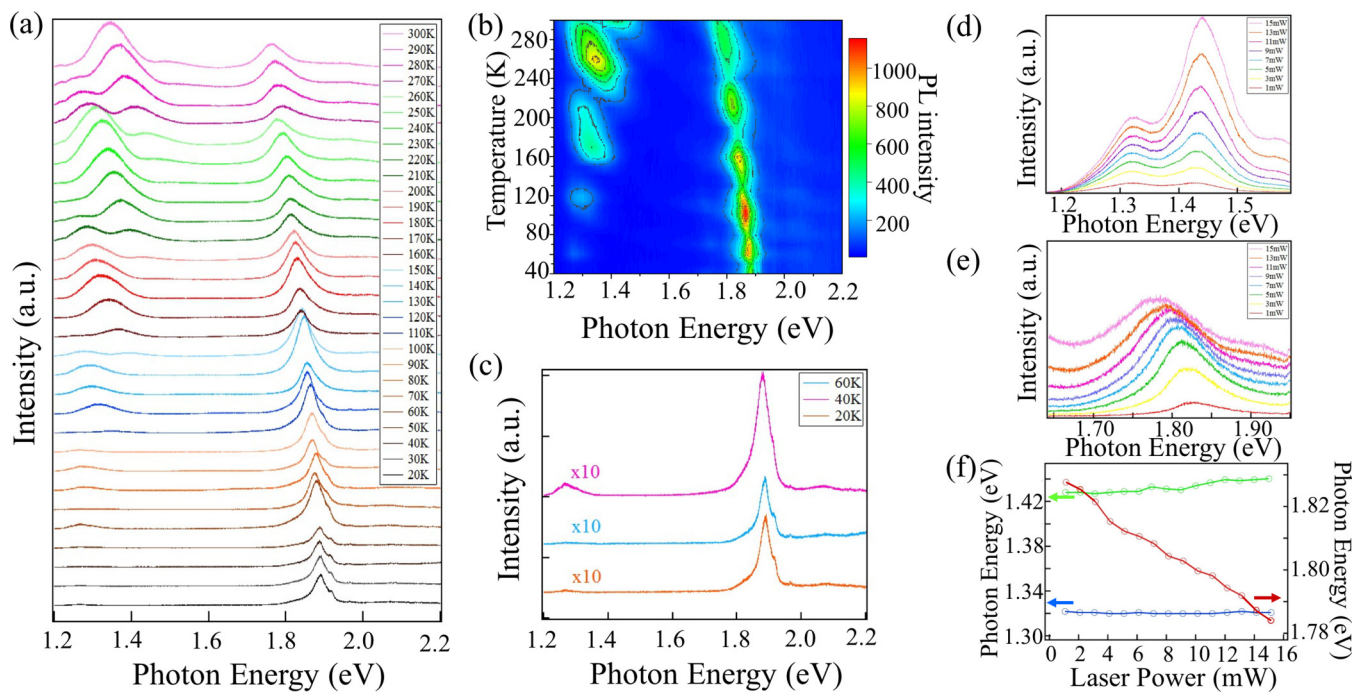

FIG. 3. Temperature dependence of PL on MoS$_2$ bubble. (a) PL spectra of a MoS$_2$ bubble in the temperature range from 20 K to 300 K. (b) 2D mapping image of PL intensity in (a), from which we can observe the peak at ~1.8 eV shows a redshift. (c) Three PL spectra of MoS$_2$ bubble measured at 20 K, 40 K, and 60 K. (d),(e) Laser power dependent of the indirect- and direct-gap PL spectra of another multilayer MoS$_2$ bubble. (f) Peak position variation with increasing laser power for the two indirect-gap PL peaks at ~1.3 eV, ~1.4 eV, and one direct-gap PL peak at ~1.8 eV.
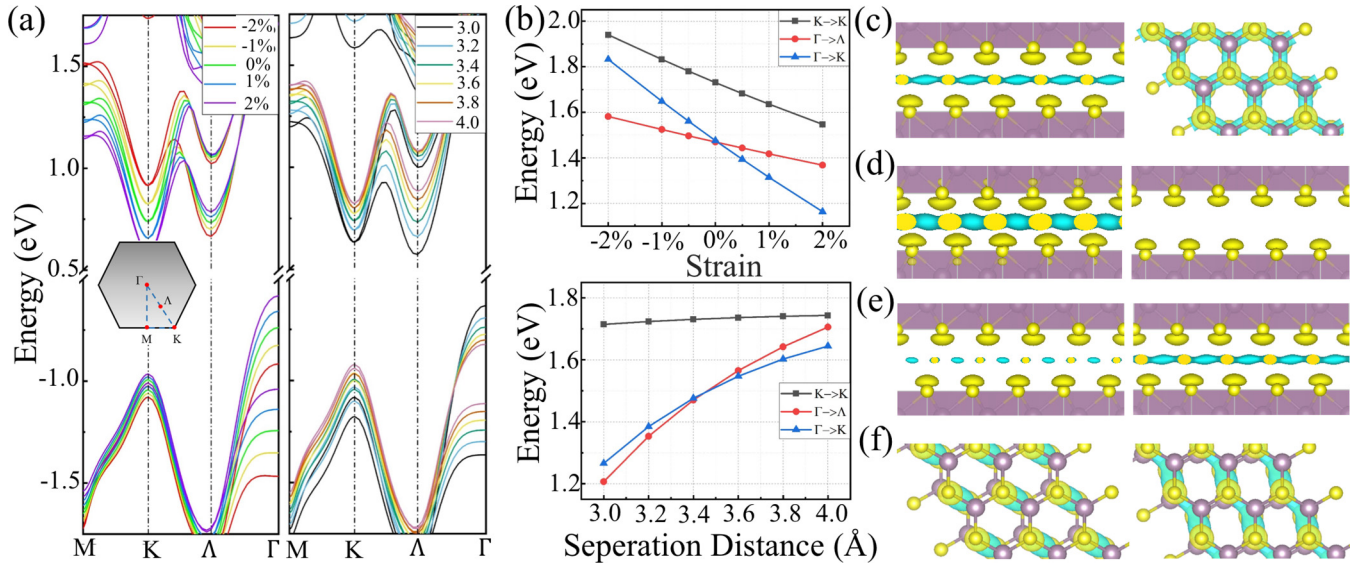
FIG. 4. Band structure calculations on the origin of PL peaks on MoS$_2$ bubble. (a) Band structures of bilayer MoS$_2$ with different strain (left) and interlayer distance (right). (b) Statistical diagram of band gap dependence of bilayer MoS$_2$ as a function of strain (upper) and interlayer distance (lower). (c) Strain-free bilayer MoS$_2$ with 3.8 Å separation of sulfur atoms in neighboring layers distance is taken as a reference system. (d) Side view of charge density difference by changing the interlayer distance (left: 3.4 Å, right: 4.0 Å). (e) Side view of bilayer MoS$_2$ under biaxial tensile (left: +2%) and compressive (right: −2%) strain. (f) Interlayer shift of 0.5 Å along armchair (left) and zigzag (right). All the plots of charge density difference have the same isosurface value of 1.45×10^{-4} e/Å.

phonon energy compared to the one at ∼1.4 eV. The different temperature-dependent behaviors of the three PL modes prove that the peak at 1.8 eV is a direct gap transition, while the other two PL modes are phonon-assisted indirect transitions. These observations are consistent with our calculation results shown below.

We observe an obvious redshift that is nearly linear for the PL peak at ∼1.8 eV as temperature increases from 20 K to 300 K [Figs. 3(a) and 3(b)]. This trend can be described by the Varshni equation [23,24]:

$$E_g(T) = E_g(0) - \alpha \times T^2/(T + \beta^2) \quad (1)$$

which shows the direct band-gap change as a function of temperature. In this equation, $E_g(T)$ is the energy gap, $E_g(0)$ is its value at 0 K, and α and β are constants. In addition, all the three peaks show intensity oscillation as shown in Fig. 4(b). As temperature increases from 20 K to 300 K, the bubble also gradually expands since the trapped gas pressure increases with temperature (shown in Fig. S7). As a result, the intensity of PL peaks show maxima and minima oscillation alternately as the height of the bubble increases when the sample warms up.

The above temperature-dependent PL measurements, for a given position, simultaneously change both the local temperature and strain. To isolate only the temperature effect, we performed laser power dependent PL measurements on the bubble. The laser is focused on the bubble with a spot size of ∼500 nm. In this case, the local temperature increases with increasing power, while the strain change is negligible. Figures 3(d) and 3(e) show PL peaks of one MoS$_2$ bubble under different laser powers. The laser power range from 1 mW to 15 mW, and the step is 2 mW. The bubbles can easily break once the laser power higher than 15 mW. We

find that the positions of the two indirect-gap PL peaks show a small energy shift, but the direct-gap PL peak obviously moves to lower photon energy as the laser power increases [Fig. 3(f)], indicating that the direct band gap becomes smaller as temperature increases, which is consistent with previous reports [24]. We also observe that the intensity of indirect-gap PL peaks, especially the one at 1.4 eV, increases linearly with increasing laser power (Fig. S8). These results prove that the position of indirect PL peaks independent with temperature. However, the intensity of the two peaks is clearly enhanced since more indirect PL transitions were activated by phonons as temperature increasing.

To further reveal the origin of the three PL transitions on multilayer MoS$_2$ bubbles, we performed first-principle band structure calculations. The band structures of bilayer MoS$_2$ are calculated by varying the in-plane biaxial strain [left panel in Fig. 4(a)] and the interlayer distance [right panel in Fig. 4(a)], respectively. We found that three electronic excitations, namely direct transition at K point, indirect transitions at $\Gamma \to K$ and $\Gamma \to \Lambda$, are dominant around the Fermi level [Fig. 4(a)]. Their band gaps decrease as the lattice biaxial strain increases with constant interlayer separation. On the other hand, the indirect excitation gaps increase significantly and the direct excitation gap increases just slightly as the interlayer separation increases [Fig. 4(b)]. The contrasting behavior between the biaxial strain and interlayer separation also emerges in six-layer MoS$_2$ (Fig. S9). When the bilayer MoS$_2$ has equilibrium interlayer separation, the tensile strained bilayer MoS$_2$ with smaller interlayer separation has indirect gap excitation of 1.30 eV and 1.45 eV, which is in agreement with experimental PL data [Fig. 1(d)]. We found that the direct band gap transition of 1.73 eV in bilayer MoS$_2$ at K point has little dependence on the interlayer separation
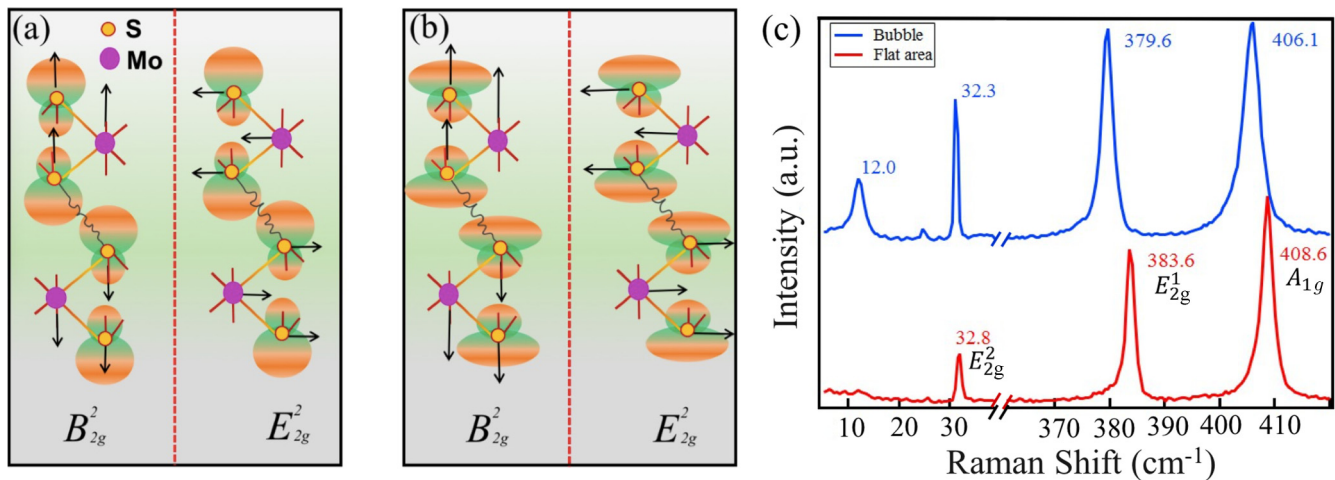
FIG. 5. High- and low-frequency Raman behaviors of multilayer MoS$_2$ bubble. (a) Lattice structure and linear chain models of AB stacked flat MoS$_2$. The layer breathing (B_{2g}^2) and shear modes (E_{2g}^2) are marked by arrows. The schematic charge density structures of p_z orbitals are presented on sulfur atoms. (b) The charge density distribution of p_z orbitals is suppressed along Z direction and spread into XY plane under tensile strain. (c) Raman spectra measured at higher (>370 cm^{-1}) and lower (<50 cm^{-1}) frequency region on multilayer MoS$_2$ bubbles and flat area.

even at larger lattice strain. Although our calculations are performed without considering the electron-hole interaction and spin-orbit coupling, the strain dependence of band gap will not be affected, therefore, the calculation results can be well applied to explain the unusual PL behavior of multilayer MoS$_2$ bubbles.

Furthermore, we can calculate charge density differences defined by $\Delta\rho = \rho_{\text{bilayer}}$-$\rho_{\text{top}}$-$\rho_{\text{bottom}}$, where ρ_{bilayer}, ρ_{top}, ρ_{bottom} are the total charge density of the bilayer MoS$_2$, the separate charge density of top layer and bottom layer charge density, respectively. Here, we choose a bilayer MoS$_2$ with 3.8 Å interlayer distance [Fig. 4(c)]. Figures 4(d)–4(f) show the charge density difference between layers under a smaller (3.4 Å) and larger (4.0 Å) interlayer distance, tensile (+2%) and compressive (−2%) strain, and layer shift in armchair and zigzag (0.5 Å) directions. The interlayer charge density becomes depleted when applying tensile strain or increasing the interlayer distance. On the multilayer MoS$_2$ bubble, a tensile strain is applied on the MoS$_2$ lattice, and the interlayer distance can also be increased. As shown above, the tensile strain and increased interlayer separation can weaken the interlayer coupling in multilayer MoS$_2$ bubble, therefore, some monolayerlike behaviors become observable on the multilayer bubble structure.

In order to figure out the mechanism of PL, one needs to compare the differences of lattice and electron structures between flat MoS$_2$ and bubble. Bubble structure applies tensile strain on the multilayer MoS$_2$, which enlarges its lattice constant. In addition, the deformation of neighboring layers are different, so there will be sliding between layers, resulting in a change of the shear mode in the multilayer. Raman spectroscopy is then used to characterize the strain and interlayer shear, which has been a prime nondestructive characterization tool for graphene [25,26] and other layered materials [27,28].

The high-frequency (>370 cm^{-1}) Raman spectra of bulk 2H-MoS$_2$ are primarily characterized by A_{1g} (408.6 cm^{-1}) and

E_{2g}^1 (383.6 cm^{-1}) modes. The A_{1g} mode originates from the out-of-plane vibration of sulfur atoms in a layer in opposite directions, while the E_{2g}^1 mode is the in-plane optical vibration of molybdenum atoms and sulfur atoms [6,28,29]. Previous reports indicate that A_{1g} and E_{2g}^1 peaks of tensile strained monolayer MoS$_2$ show obvious redshifts [6,20,30]. Here, we also observed redshifts for E_{2g}^1 (4 cm^{-1}) and A_{1g} (2.5 cm^{-1}) peaks on tensile strained multilayer MoS$_2$ bubble in comparison with strain-free flat area, as shown in the right part of Fig. 5(c). The frequency shift of mode on the bubble clearly illustrates that this mode is significantly affected by in-plane strain. As reported in previous studies, the Raman peak of few-layer MoS$_2$ is redshifted by 1.7 cm^{-1}/% under uniaxial tensile strain [9,30], from which we can estimate the strain on the bubble [Fig. 1(b)] is about 2.35%. This result is consistent with strain value obtained by AFM. The double degenerate mode on multilayer MoS$_2$ bubble dose not split, which is different from the behavior exhibited by 1L or 2L-MoS$_2$ under uniaxial tensile strain [6,30,31].

In the Raman spectrum of multilayer MoS$_2$, the E_{2g}^2 and B_{2g}^2 modes at the low-frequency range (<50 cm^{-1}) are sensitive to shear and layer breathing vibration [28]. The peak position can be used to characterize interlayer coupling force, while the intensity of Raman peak can help gauge the strength of electron-phonon coupling (EPC) [32–36]. As shown in Fig. 5(a), we present the lattice structure and linear chain models of AB stacked flat MoS$_2$. The charge density distributions of p$_z$ orbitals of sulfur atoms are also provided in this image. In fact, the interlayer coupling between MoS$_2$ layer is mainly contributed by p$_z$ orbitals of S atoms. Once a bubble is formed, a biaxial tensile strain is generated on multilayer MoS$_2$. In this case, the length of Mo-S bonds will be lengthened, therefore, the charge density distributions of p$_z$ electrons can be changed [Fig. 5(b)]. Specifically, the charge density distribution of p$_z$ orbital of S atoms can be more extended along the in-plane direction, so the distribution on Z direction is suppressed

compared with the flat MoS_2 area. Meanwhile, the intensity of coupling interaction can be described by the restoring force of a whole layer when the horizontally or vertically relative displacements occur between two adjacent layers. According to previous studies, the shift of low-frequency Raman peak can be used to characterize the change of interlayer coupling force quantitatively [28,32–34]. As shown in Fig. 5(c), the B_{2g}^2 and E_{2g}^2 modes redshift from 12.5 cm^{-1} to 12.0 cm^{-1} and from 32.0 cm^{-1} to 31.1 cm^{-1}, respectively. According to the linear chain model [28,32–34], we can conclude that lower frequency means smaller coupling force constant based on same layer numbers. Specifically, the out-of-plane force constant K_z and in-plane force constant K_x on bubble are 7.8% and 5.5% smaller than in flat area, respectively. The intensity of low frequency Raman modes can also reflect some EPC-related properties [35]. EPC can be ascribed to the interaction between B_{2g}^2 and E_{2g}^2 phonons with electrons of specific orbitals. The B_{2g}^2 mode involves out-of-plane vibration of S atoms and, therefore, it is expected to modulate the d_{z^2} orbitals of Mo atoms strongly. As for the shear mode, the in-plane movements of S atoms modulate the p_x and p_y electron clouds of S atoms. Raman intensity can be calculated by the third-order time dependent perturbation theory [35,36], from which we know that the Raman intensity is proportional to the square of the matrix element associated with electron-phonon interaction. As can be seen in Fig. 5(c), the intensities of B_{2g}^2 and E_{2g}^2 modes on the bubble are 3.0 and 5.7 times higher than those of the flat area, respectively, indicating that the EPCs become stronger. The low frequency Raman results are consistent with our calculation results, which unambiguously demonstrate that the interlayer coupling is weakened and the EPC is strengthened on multilayer MoS_2 bubble in comparison with flat area. As a result, the multilayer MoS_2 bubble structure presents some new phenomena which are different from both flat monolayer and multilayer, such as the emergence of PL peaks shown in Fig. 1(c).

IV. SUMMARY

In summary, we observed both direct- and indirect-gap PL emissions in multilayer MoS_2 bubbles. Larger MoS_2 bubbles (diameter >5 μm) show PL oscillation in the mapping images owing to the interference effect generated by the bubble structure. From temperature-dependent PL measurements, we verified that the two peaks at around 1.3 and 1.4 eV are phonon-assisted indirect-gap transitions and the peak at ∼1.8 eV is due to direct gap transition. Moreover, the direct-gap PL exhibits a redshift as the temperature increases. The first-principle band structure calculations revealed the evolution of the band structure of multilayer MoS_2 with strain and interlayer separation, which clarified the origin of the three PL peaks on the bubble. The weakening of interlayer coupling on multilayer MoS_2 bubbles, which is confirmed by the redshift of low-frequency Raman spectroscopy, can be responsible for the emergence of the three PL peaks. Multilayer MoS_2 bubbles provide a new platform for understanding the band structure evolution and optical property changes of this material under strain. This work can deliver new inspiration for the field of light-emitting diodes and photodetectors based on multilayer TMDCs.

V. METHODS

A. Experiments

Fabrication of MoS_2 bubbles. Before exfoliating thin MoS_2, the SiO_2/Si substrate was exposed to oxygen plasma to remove adsorbates from its surface. Following this step, the MoS_2-loaded tape adhered to the substrate and the substrate was heated for $1 \sim 2$ min at ∼110 °C in air. Since the substrate surface can absorb small molecules in air, the interface between MoS_2 and the substrate traps some of these gas molecules. These molecules can then accumulate at the interface and form bubble structures when being heated on a hot plate. After the sample cooled to room temperature, the adhesive tape was removed and bubbles with different sizes were fabricated [18].

B. AFM, Raman, and PL measurements

Atomic force microscopy (Park, XE7) and confocal Raman spectroscopy/microscopy (WITec alpha 300) were used to measure the properties and thickness of exfoliated MoS_2. A laser wavelength of 532 nm and spot size of ∼0.5 μm was used to obtain Raman/PL spectra and spatially resolved Raman/PL mapping images. In the temperature dependent PL measurement, the MoS_2 bubble sample was loaded in a homemade vacuum chamber with temperature control system. The temperature can be continuously controlled from 20 K to room temperature.

C. Calculations

Density functional theory calculations. All first-principle calculations are performed on the base of density functional theory (DFT [37,38]) via Vienna *ab initio* simulation package (VASP) [39]. We used the local density approximation (LDA [40]) form for exchange-correction functional to calculate the charge distribution and electronic structure of bilayer MoS_2. Ion cores are described by using the projector-augmented wave (PAW [41]) method. A $9 \times 9 \times 1$ k-point grid generated by Monkhorst-Pack is used. The energy cutoff is set to be 500 eV. The spin-orbit coupling (SOC) has been included as well.

[1] A. Splendiani, L. Sun, Y. Zhang, T. Li, J. Kim, C.-Y. Chim, G. Galli, and F. Wang, Nano Lett. **10**, 1271 (2010).

[2] S. Mukherjee, R. Maiti, A. K. Katiyar, S. Das, and S. K. Ray, Sci. Rep. **6**, 29016 (2016).

[3] W. J. Zhao, R. M. Ribeiro, M. L. Toh, A. Carvalho, C. Kloc, A. H. Castro Neto, and G. Eda, Nano Lett. **13**, 5627 (2013).

[4] J. Lee, L. Tao, K. N. Parrish, Y. Hao, R. S. Ruoff, and D. Akinwande, Appl. Phys. Lett. **101**, 252109 (2012).

[5] J. W. Suk, K. Kirk, Y. Hao, N. A. Hall, and R. S. Ruoff, Adv. Mater. **24**, 6342 (2012).

[6] C. R. Zhu, G. Wang, B. L. Liu, X. Marie, X. F. Qiao, X. Zhang, X. X. Wu, H. Fan, P. H. Tan, T. Amand, and B. Urbaszek, Phys. Rev. B **88**, 121301(R) (2013).

[7] H. J. Conley, B. Wang, J. I. Ziegler, R. F. Haglund, S. T. Pantelides, and K. I. Bolotin, Nano Lett. **13**, 3626 (2013).

[8] K. He, C. Poole, K. F. Mak, and J. Shan, Nano Lett. **13**, 2931 (2013).

[9] A. Castellanos-Gomez, R. Roldan, E. Cappelluti, M. Buscema, F. Guinea, H. S. J. van der Zant, and G. A. Steele, Nano Lett. **13**, 5361 (2013).

[10] Z. Dai, Y. Hou, D. A. Sanchez, G. Wang, C. J. Brennan, Z. Zhang, L. Liu, and N. Lu, Phys. Rev. Lett. **121**, 266101 (2018).

[11] E. Khestanova, F. Guinea, L. Fumagalli, A. K. Geim, and I. V. Grigorieva, Nat. Commun. **7**, 12587 (2016).

[12] Y. Huang, X. Wang, X. Zhang, X. Chen, B. Li, B. Wang, M. Huang, C. Zhu, X. Zhang, W. S. Bacsa, F. Ding, and R. S. Ruoff, Phys. Rev. Lett. **120**, 186104 (2018).

[13] Z. Jia, J. Dong, L. Liu, A. Nie, J. Xiang, B. Wang, F. Wen, C. Mu, Z. Zhao, B. Xu, Y. Gong, Y. Tian, and Z. Liu, Adv. Optic. Mater. **7**, 1801373 (2019).

[14] A. V. Tyurnina, D. A. Bandurin, E. Khestanova, V. G. Kravets, M. Koperski, F. Guinea, A. N. Grigorenko, A. K. Geim, and I. V. Grigorieva, ACS photonics **6**, 516 (2019).

[15] P. Jia, W. Chen, J. Qiao, M. Zhang, X. Zheng, Z. Xue, R. Liang, C. Tian, L. He, Z. Di, and X. Wang, Nat. Commun. **10**, 3127 (2019).

[16] D. Tedeschi, E. Blundo, M. Felici, G. Pettinari, B. Liu, T. Yildirim, E. Petroni, C. Zhang, Y. Zhu, S. Sennato, Y. Lu, and A. Polimeni, Adv. Mater. **31**, 1903795 (2019).

[17] L. He, H. Wang, L. Chen, X. Wang, H. Xie, C. Jiang, C. Li, K. Elibol, J. Meyer, K. Watanabe, T. Taniguchi, Z. Wu, W. Wang, Z. Ni, X. Miao, C. Zhang, D. Zhang, H. Wang, and X. Xie, Nat. Commun. **10**, 2815 (2019).

[18] Y. Huang, E. Sutter, N. N. Shi, J. Zheng, T. Yang, D. Englund, H.-J. Gao, and Peter Sutter, ACS Nano. **9**, 10612 (2015).

[19] D. Lloyd, X. Liu, J. W. Christopher, L. Cantley, A. Wadehra, B. L. Kim, B. B. Goldberg, A. K. Swan, and J. S. Bunch, Nano Lett. **16**, 5836 (2016).

[20] J. Chaste, A. Missaoui, S. Huang, H. Henck, Z. B. Aziza, L. Ferlazzo, C. Naylor, A. Balan, A. T. Charlie Johnson, R. Braive, and A. Ouerghi, ACS Nano. **12**, 3235 (2018).

[21] G. Wang, Z. Dai, Y. Wang, P. H. Tan, L. Liu, Z. Xu, Y. Wei, R. Huang, and Z. Zhang, Phys. Rev. Lett. **119**, 036101 (2017).

[22] See Supplemental Material at http://link.aps.org/supplemental/10.1103/PhysRevMaterials.4.074006 for the thickness of MoS$_2$ flake characterized by atomic force microscope.

[23] T. Korn, G. Plechinger, S. Heydrich, F.-X. Schrettenbrunner, J. Eroms, D. Weiss, and C. Schuller, *Optical Characterization, Low-Temperature Photoluminescence, and Photocarrier Dynamics in MoS$_2$. MoS$_2$: Materials, Physics, and Devices* (Springer International Publishing, Cham, 2014), pp. 217–236.

[24] Y. P. Varshni, Physica **34**, 149 (1967).

[25] A. C. Ferrari, J. C. Meyer, V. Scardaci, C. Casiraghi, M. Lazzeri, F. Mauri, S. Piscanec, D. Jiang, K. S. Novoselov, S. Roth, and A. K. Geim, Phys. Rev. Lett. **97**, 187401 (2006).

[26] A. C. Ferrari, Solid State Commun. **143**, 47 (2007).

[27] H. Zeng, B. Zhu, K. Liu, J. Fan, X. Cui, and Q. M. Zhang, Phys. Rev. B **86**, 241301(R) (2012).

[28] X. Zhang, W. P. Han, J. B. Wu, S. Milana, Y. Lu, Q. Q. Li, A. C. Ferrari, and P. H. Tan, Phys. Rev. B **87**, 115413 (2013).

[29] C. Lee, H. Yan, L. E. Brus, T. F. Heinz, J. Hone, and S. Ryu, ACS Nano. **4**, 2695 (2010).

[30] C. Rice, R. J. Young, R. Zan, U. Bangert, D. Wolverson, T. Georgiou, R. Jalil, and K. S. Novoselov, Phys. Rev. B **87**, 081307(R) (2013).

[31] J.-U. Lee, S. Woo, J. Park, H. C. Park, Y.-W. Son, and H. Cheong, Nat. Commun. **8**, 1370 (2017).

[32] Y. Zhao, X. Luo, H. Li, J. Zhang, P. T. Araujo, C. K. Gan, J. Wu, Hua Zhang, Su Ying Quek, M. S. Dresselhaus, and Q. Xiong, Nano Lett. **13**, 1007 (2013).

[33] J. B. Wu, X. Zhang, M. Ijas, W.-P. Han, X.-F. Qiao, X.-L. Li, D.-S. Jiang, A. C. Ferrari, and P.-H. Tan, Nat. Commun. **5**, 5309 (2014).

[34] P. H. Tan, W. P. Han, W. J. Zhao, Z. H. Wu, K. Chang, H. Wang, Y. F. Wang, N. Bonini, N. Marzari, N. Pugno, G. Savini, A. Lombardo, and A. C. Ferrari, Nat. Mater. **11**, 294 (2012).

[35] B. R. Carvalho, L. M. Malard, J. M. Alves, C. Fantini, and M. A. Pimenta, Phys. Rev. Lett. **114**, 136403 (2015).

[36] M. L. Lin, Y. Zhou, J.-B. Wu, X. Cong, X.-L. Liu, J. Zhang, H. Li, W. Yao, and P.-H. Tan, Nat. Commun. **10**, 2419 (2019).

[37] P. Hohenberg, Phys. Rev. **136**, B864 (1964).

[38] W. Kohn and L. J. Sham, Phys. Rev. **140**, A1133 (1965).

[39] G. Kresse and J. Furthmuller, Phys. Rev. B **54**, 11169 (1996).

[40] J. W. Negele, Phys. Rev. C **1**, 1260 (1970).

[41] M. Gajdos, K. Hummer, G. Kresse, J. Furthmuller, and F. Bechstedt, Phys. Rev. B **73**, 045112 (2006).